



**Enhanced Visible-NIR Absorption and Oxygen Vacancy
Generation of Pt/H_xMoWO_y by H-spillover to Facilitate
Photothermal Catalytic CO₂ Hydrogenation**

| | |
|-------------------------------|---|
| Journal: | <i>Journal of Materials Chemistry A</i> |
| Manuscript ID | TA-ART-02-2022-001595.R1 |
| Article Type: | Paper |
| Date Submitted by the Author: | 11-Apr-2022 |
| Complete List of Authors: | Ge, Hao; Osaka University, Division of Materials and Manufacturing Science Kuwahara, Yasutaka; Osaka University, Graduate School of Engineering, Division of Materials and Manufacturing Science Kusu, Kazuki; Osaka University, Graduate School of Engineering, Division of Materials and Manufacturing Science Kobayashi, Hisayoshi; Kyoto Institute of Technology Yamashita, Hiromi; Osaka University, Division of Materials and Manufacturing Science |
| | |

ARTICLE

Enhanced Visible-NIR Absorption and Oxygen Vacancy Generation of Pt/H_xMoWO_y by H-spillover to Facilitate Photothermal Catalytic CO₂ Hydrogenation

Received 00th January 20xx,
Accepted 00th January 20xx

DOI: 10.1039/x0xx00000x

Hao Ge,^a Yasutaka Kuwahara,^{*a,b,c,d} Kazuki Kusu,^a Hisayoshi Kobayashi,^{a,e} Hiromi Yamashita^{*a,b,c}

Photothermal catalytic hydrogenation of CO₂ is an intriguing approach to reduce CO₂ under mild conditions, which is possible because of photoinduced electron-hole pair generation and an overall increase of the localized temperature under light irradiation. However, the lack of a catalyst with an adequate photothermal conversion efficiency and the ability to generate a sufficient number of photoinduced electrons is the main factors limiting the applicability of this method. H-doped WO₃ demonstrates surface plasmon resonance (SPR) capabilities, and can be adjusted by changing the dopant (H⁺) concentration. To improve the potential of the WO₃ plasmonic effect based on H-doping, we herein report that the Mo-doped Pt/WO₃ (Pt/MoWO₃) substantially increases the dopant (H⁺) and oxygen vacancy concentration in Pt/H_xMoWO_y during the H₂ reduction process, facilitating photothermal hydrogenation of CO₂ to CO. The developed Pt/H_xMoWO_y exhibits excellent catalytic performance (3.1 mmol h⁻¹ g⁻¹) in the photothermal reverse water-gas shift (RWGS) reaction at 140 °C, outperforming undoped Pt/H_xWO₃ (1.02 mmol h⁻¹ g⁻¹). Experimental and comprehensive analyses, including photoelectrochemical measurements, UV-vis-NIR diffuse-reflectance spectroscopy, and a model reaction, showed that abundant surface free electrons and oxygen vacancies (V_O) in Pt/H_xMoWO_y are responsible for the efficient CO₂ adsorption and transfer of photoinduced electrons to carry out the reduction of CO₂ to CO. X-ray photoelectron spectroscopy (XPS) and in situ X-ray absorption fine structure (XAFS) measurements revealed a reversible redox event for the Mo and W atoms during the RWGS reaction, confirming that the oxygen vacancies between Mo and W atoms in Pt/H_xMoWO_y act as active sites and that Pt nanoparticles activate H₂ to enable the regeneration of the oxygen vacancies. Moreover, density functional theory (DFT) calculations demonstrated that Mo-doping substantially decreases the energy barrier for oxygen vacancy formation in WO₃ in H₂ reduction process. We expect this study provides an innovative strategy for designing a highly efficient catalyst for photothermal CO₂ conversion.

Introduction

The unstoppable rise of carbon dioxide (CO₂) level in the atmosphere have already reached 419 ppm as of 2021, posing a huge threat to the sustainable development of human society. The control and reduction of CO₂ emissions have attracted the attention of leaders and researchers worldwide. Under the concept of sustainable development, carbon capture and utilization (CCU) technology could be an effective breakthrough.¹⁻³ CO₂ conversion into value-added chemicals and fuels is recognized as a promising technique for CO₂ mitigation and energy regeneration.⁴⁻⁶ Using reverse water gas shift (RWGS) reaction to obtain high-purity CO from CO₂ is an attractive strategy because the generated CO can be used as

raw material in Fischer-Tropsch synthesis to produce various hydrocarbons and fundamental chemicals.⁷ This reaction is endothermic with a standard heat of reaction of 41.27 kJ mol⁻¹, as shown in Eq (1).



The traditional thermal catalytic conversion of CO₂ to CO is an energy-intensive approach, that relies on precious (e. g., Pt and Pd) and nonprecious (e.g., Cu and Fe) metals immobilized on oxides as catalyst supports.⁸⁻¹¹ However, thermal catalysis is usually carried out under severe conditions (1-4 MPa and 200-400 °C) to achieve a high CO production rate, thereby consuming a large amount of nonrenewable energy.¹²⁻¹⁴ To mitigate the consumption of non-renewable energy in the RWGS reaction, photothermal catalytic technology has been demonstrated as a reasonable concept. Unlike thermal catalysis, the photothermal effect mainly relies on non-radiative decay to enhance the photogeneration of electron-hole pairs to simultaneously drive thermochemical and photochemical process on the catalyst surface.¹⁵ Recently, photothermal CO₂ hydrogenation for CO production at atmospheric pressure and temperature (< 200 °C) has been widely reported. For example, Ouyang *et al.* reported that the use of black In₂O₃ with a high oxygen vacancy density led to a substantial increase in the CO production rate with 100% selectivity at room temperature, achieving high-performance solar-to-chemical energy

^a Division of Materials and Manufacturing Science, Graduate School of Engineering, Osaka University, 2-1 Yamada-oka, Osaka 565-0871, Japan

^b Institute for Open and Transdisciplinary Research Initiatives (OTRI), Osaka University, 2-1 Yamada-oka, Suita, Osaka 565-0871, Japan

^c Unit of Elements Strategy Initiative for Catalysts & Batteries (ESICB), Kyoto University, Katsura, Kyoto 615-8520, Japan

^d JST, PRESTO, 4-1-8 Hon-cho, Kawaguchi, Saitama 332-0012, Japan

^e Kyoto Institute of Technology, Matsugasaki, Sakyo-ku, Kyoto 606-8585, Japan

*E-mail: kuwahara@mat.eng.osaka-u.ac.jp (Y. Kuwahara);

yamashita@mat.eng.osaka-u.ac.jp (H. Yamashita)

Electronic Supplementary Information (ESI) available: [details of any supplementary information available should be included here]. See DOI: 10.1039/x0xx00000x

conversion.¹⁶ Li *et al.* demonstrated that Ni/Nb₂C exhibits excellent photothermal conversion ability, resulting in an outstanding CO yield in a CO₂ hydrogenation reaction under intense illumination without external heating.¹⁷ Thus, the development of photothermal catalysts with excellent CO₂ conversion performance under mild reaction conditions is an emerging interest.^{18,19}

Tungsten oxide (WO₃) has been demonstrated as a promising photocatalyst because of its potential for visible-to-near-infrared (Vis-NIR) light absorption and utilization. This property is attributable to the ability of WO₃ to form hydrogen bronze (H_xWO_{3-y}), which contains free electrons and oxygen vacancies (V_O) in its lattice.²⁰⁻²² Notably, WO₃ has a unique surface plasmon resonance (SPR) property that enables it to utilize solar energy in the Vis-NIR region.²³ Ishihara *et al.* synthesized ultrathin WO₃·0.33H₂O nanotubes with abundant localized electrons, enhancing the Vis-NIR light absorption and enabling stable photoreduction of CO₂ to CH₃COOH in an aqueous medium.²⁴ A literature survey revealed that Pd/WO₃ can generate oxygen vacancies and free electrons after H₂ reduction at 300 °C, exhibiting a greatly enhanced CO₂ conversion performance (~2 folds) under illumination with a 300 W Xe arc lamp compared with the conversion performance under dark condition; oxygen vacancies in the Pd/WO₃ function as active sites for CO₂ reduction.²⁵ Increasing the concentration of free electrons and the number of defects in WO₃ is a critical step for enhancing the CO yield in the photothermal catalytic reduction of CO₂.

Charge-carrier densities in semiconductors can be modulated by aliovalent ion doping, which leads to the emergence of SPR in certain metal oxides.²⁶⁻²⁸ For example, Sn-doped In₂O₃ (ITO) exhibits strong plasmon oscillation absorption in the NIR region, because the Sn dopant increases the density of free electrons in the conduction band.²⁹ In addition, aliovalent ion doping creates a larger number of defects (such as oxygen vacancies) in the lattice and thereby changes the valence state of an element in an oxide, providing an opportunity to promote the adsorption of target reactants and the utilization of photoinduced electrons.^{30,31} Wang *et al.* reported that the doping Mo atoms into WO_x can promote photoinduced electron-hole pair separation and facilitate the transfer of photoinduced electrons from active sites to CO₂, thereby increasing the efficiency of the photoreduction of CO₂ to CH₄.³² Xiong *et al.* demonstrated that doping Mo⁵⁺ into WO_x nanowires can create massive defects (oxygen vacancies), resulting in the centers of Mo-W moieties being the active sites for the chemisorption of N₂ molecules. The enhanced metal-oxygen covalency in the photocatalyst lattice facilitates the photoinduced electron transfer to N₂ molecules to promote ammonia production.³³ In this context, we previously reported that the generation of abundant delocalized electrons in the Mo 4*d* band via H₂ reduction of α-MoO₃ confers metal/H_xMoO_{3-y} with a plasmonic feature in the Vis-NIR light region and that this promotes several chemical reactions with the aid of light energy; we also found that the intensity of plasmonic absorption can be adjusted by controlling the H₂ reduction temperature.³⁴⁻³⁷ In addition, the oxygen vacancies (V_O) in Pt/H_xMoO_{3-y} provide effective sites for

activating molecular CO₂ and weakening the C=O bonds, facilitating the generation of CO in the photothermal catalytic CO₂ reaction, while Pt nanoparticles (NPs) act as H₂ dissociation sites, continuously supplying active H atoms to increase the concentration of free electrons in MoO₃ and regenerating the oxygen vacancies.^{38,39} Given the foregoing background information, Mo-doped Pt/WO_y can be expected to enhance the number of defects (oxygen vacancies) and the free electron (H⁺) concentration via H₂ reduction to facilitate CO₂ activation and solar energy utilization, realizing highly efficient photothermal catalytic CO₂ reduction.

In the present work, we developed a heavily H-doped Pt/H_xMoWO_y catalyst based on H₂ reduction process, exhibits a high CO production rate in the photothermal catalytic hydrogenation of CO₂ under relatively mild reaction conditions (reaction temperature: 140 °C; light intensity: 0.88 W cm⁻²; light source: Vis-NIR). During the H₂ reduction process, the Mo-doping can critically and concurrently promote intercalation of H atoms and generation of oxygen vacancy in Pt/MoWO_y, which enhance CO₂ chemisorption, plasmonic absorption, photoinduced electron transfer and photothermal conversion efficiency of Pt/H_xMoWO_y in the photothermal catalytic reaction. Photoelectrochemical measurements reveal that Pt/H_xMoWO_y can generate more photoinduced electrons than undoped Pt/H_xWO_y, and that these electrons are efficiently transferred from Pt/H_xMoWO_y to the chemisorbed CO₂. The plasmonic absorption in the NIR region, in particular, enables Pt/H_xMoWO_y to achieve a superior CO yield. This work proposes a feasible strategy for designing and developing a high-performance photothermal CO₂ hydrogenation catalyst that utilizes solar energy in the Vis-NIR region to overcome the CO₂ activation constraints.

Experimental

Materials

Ammonium molybdate tetrahydrate (NH₄)₆Mo₇O₂₄·4H₂O, 99.0%), tungsten (VI) oxide (WO₃) were purchased from Wako Pure Chemical Industries. Potassium tetrachloroplatinate(II) (K₂PtCl₄) and tungsten(VI) chloride (WCl₆) were purchased from Nacalai Tesque, and MoCl₅ was purchased from Sigma Aldrich.

Synthesis of WO_y and Mo-doped WO_y

The Mo-doped WO_y nanowires were prepared by a simple previously reported solvothermal method.³³ First, 100 mg of WCl₆ was dissolved into 34 mL of ethanol and stirred for 30 min to obtain a transparent yellow solution. Subsequently, 1 mL of ethanol solution containing different amounts of MoCl₅ was dropped into the solution, and the resultant solution was further stirred for 10 min. The solution was then transferred into a 45 mL stainless-steel autoclave and maintained at 200 °C for 16 h. The obtained precipitate was washed three times with ethanol and dried at 25 °C in a vacuum oven overnight. The Mo-doped WO_y nanowire samples were named as MoWO_y(z) (z = 5, 10, 20, 30, 40), where z represents the molar ratio of the doped Mo relative to W (Mo: W = 5, 10, 20, 30, or 40: 100). The pure

WO_y nanowires were synthesized using the afore mentioned method but without adding MoCl₅.

Synthesis of Pt/H_xWO_y and Pt/H_xMoWO_y

500 mg of as-prepared MoWO_y nanowires was added into 50 mL of ethanol solution to form a suspension. Then, 2.5 mL of as-prepared K₂PtCl₄ solution (6 mg mL⁻¹) was added. The suspension was maintained at 70 °C under stirring for 3 h. The product was filtered and then washed with absolute ethanol; the product was then dried at 25 °C in a vacuum oven. The prepared samples were named Pt/WO_y and Pt/MoWO_y(z) (z = 5, 10, 20, 30, 40). The Pt/MoWO_y and Pt/WO_y were subsequently reduced at 200 °C for 1 h under flowing H₂ (20 mL min⁻¹); the resultant compounds were named Pt/H_xMoWO_y(z) and Pt/H_xWO_y, respectively. In the subsequent tests all Pt/H_xMoWO_y represents Pt/H_xMoWO_y(30).

Electrochemical Measurements

The photocurrent measurement was performed by a three electrodes system with a potential of 0 V (vs. Ag/AgCl) using an HS-5000 electrochemical measurement system in 0.1 M Na₂SO₄ solution. Ag/AgCl electrode and Pt wire were used as the reference electrode and the counter electrode, respectively. A mixture containing 5 mg of the catalyst with 1.5 mL of ethanol, 0.5 mL of deionized water, and 100 μL of Nafion (5%) was prepared. The working electrode was prepared by placing 30 μL of the mixture on the FTO conductive glass. Different gases and mixtures (H₂, H₂ +CO₂, CO₂, air) were flowed into the photoelectrochemical cell during the measurement depending on the experimental requirements.

The charge carrier density (ND) was calculated using the following equation:

$$N_D = \frac{2}{e\epsilon\epsilon_0} \left[\frac{d\left(\frac{1}{C^2}\right)}{dV_s} \right]^{-1} \quad (2)$$

The electronic charge (e) is 1.6 × 10⁻¹⁹ C, vacuum permittivity (ε₀) is 8.86 × 10⁻¹⁴ F cm⁻¹ and relative permittivity (ε) of WO_y is assumed to be 8.69.⁴⁰ The space-charge capacitance C [F cm⁻²] and the applied potential V_s [V] were obtained from the corresponding Mott-Schottky curves.

The decrease rate of current density was calculated using the following equation:

$$\text{Decrease rate} = \frac{\text{Current density}_{H_2} - \text{Current density}_{CO_2}}{\text{Current density}_{H_2}} \quad (3)$$

Characterization

A Rigaku Ultima IV diffractometer equipped with a Cu Kα radiation source was employed to obtain X-ray diffraction (XRD) patterns. Field emission scanning electron microscope (FE-SEM) images were recorded on a JEOL JSM-6500. High-resolution transmission electron microscopy (HR-TEM) images were recorded on a JEOL ARM200F instrument operated at 200 kV accelerating voltage. The catalyst dispersed in the ethanol was dropped onto a Cu grid covered with carbon film in Ar atmosphere to avoid sample oxidation. UV-vis-NIR diffuse-reflectance spectra were obtained by a Shimadzu UV-2600 spectrophotometer equipped with an integrating sphere, and

BaSO₄ was employed as a reference. The Kubelka–Munk function was employed to calculate the absorption intensity. A Shimadzu ESCA 3400 equipped with a Mg Kα radiation source was used to measure the XPS spectra. The whole process of introducing samples into the XPS analysis chamber was carried out in Ar atmosphere to avoid catalyst oxidation. Binding energies of the C 1s peak at 284.5 eV were used for calibration. The Mo K-edge XAFS measurements were performed in transmission mode at the BL01B1 beamline of SPring-8 (JASRI), Hyogo, Japan. A Si (311) double-crystal monochromator was employed during the measurement. For pseudo *in situ* XAFS measurement, all sample pellets were reduced in a H₂ flow before measurement and sealed in a polyethylene bag to avoid oxidation in air. For *in situ* Mo K-edge XAFS measurement, the Pt/MoWO_y sample (φ7 mm) was placed in a quartz cell (Makuhari Rikagaku Garasu Inc.) equipped with a cold water condenser and an electric heater. The sample was first reduced at 200 °C under a flow of 20% H₂/He (100 mL min⁻¹), then decreasing the temperature to 140 °C, and sequentially exposed to the flow of 50% CO₂/He (100 mL min⁻¹) and 20% H₂/He (100 mL min⁻¹) into the quartz cell. During these processes, the changes of XAFS spectra were recorded in transmission mode. The H₂ temperature-programmed reduction (H₂-TPR) measurements were performed on a BELCAT-II system (MicrotracBEL Corp.). TPR profiles were obtained at a heating rate of 5 °C min⁻¹ and with a 5 vol% H₂/Ar flowing at 30 mL min⁻¹.

DFT Calculation

The plane-wave based density functional theory (DFT) simulations were performed with the CASTEP program in Materials Studio 17.2. The generalized gradient approximation

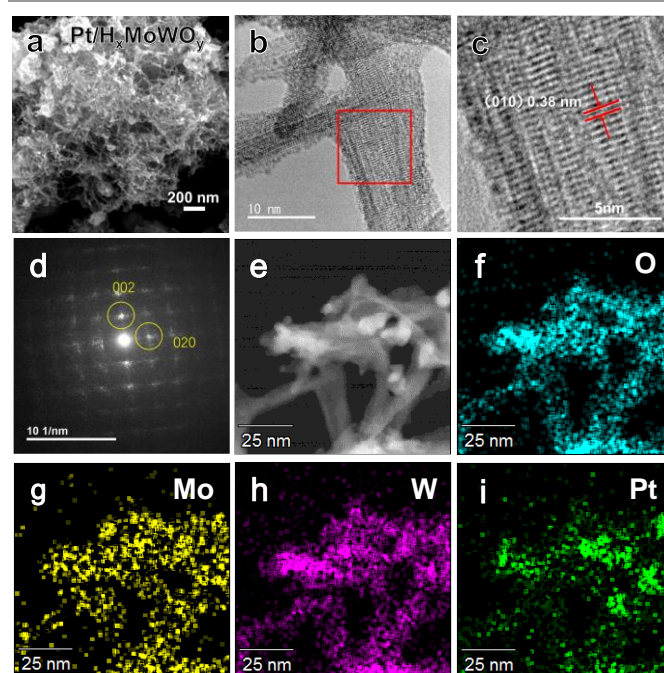


Fig. 1 (a) FESEM image of the Pt/H_xMoWO_y (30 mol% Mo doped Pt/WO_y, reduced by H₂ at 200 °C), (b) and (c) HRTEM images of Pt/H_xMoWO_y, (d) Selected-area electron diffraction pattern of Pt/H_xMoWO_y, (e) STEM image and (f-i) EDS elemental mapping images of Pt/H_xMoWO_y, for (f) O, (g) Mo, (h) W and (i) Pt atoms.

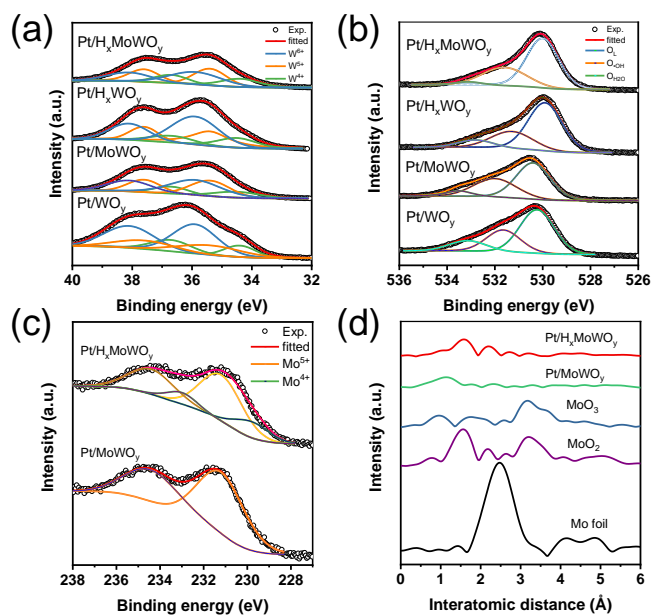


Fig. 2 XPS spectra of Pt/WO_y, Pt/MoWO_y, Pt/H_xWO_y, and Pt/H_xMoWO_y: (a) W 4f, (b) O 1s, and (c) Mo 3d; (d) FT-EXAFS spectra at the Mo K-edge of Pt/MoWO_y and Pt/H_xMoWO_y.

(GGA) of the Perdew Burke Ernzerhof (PBE) functional with the ultrasoft core potential was employed. The basis set cutoff energies were set to 300 and 340 eV for the geometry optimization and the post energy refinement. The monoclinic W₁₈O₄₉ unit cell with the lattice parameters, $a = 14.199 \text{ \AA}$, $b = 3.859 \text{ \AA}$, $c = 18.287 \text{ \AA}$, $\alpha = \gamma = 90^\circ$, and $\beta = 109.7^\circ$ was employed for the bulk, and then the (100) oriented slab models were built by cleaving at the ab facet. Two slab models, W₃₆O₉₄ and Mo₁₁W₂₅O₉₄ were built by doubling the b direction and deleting four O atoms at the boundary. The adsorption energy (E_{ads}) was defined as $E_{\text{ads}} = E_{\text{total}} - (E_{\text{sub}} + E_{\text{molecule}})$, where E_{total} , E_{sub} , and E_{molecule} are the total energies of the substrate optimized together with the adsorbate, the free substrate, and a free adsorbate molecule, respectively. The activation energy for the transition state (TS) was defined as the energy difference between the TS and the local minimum immediately before the TS.

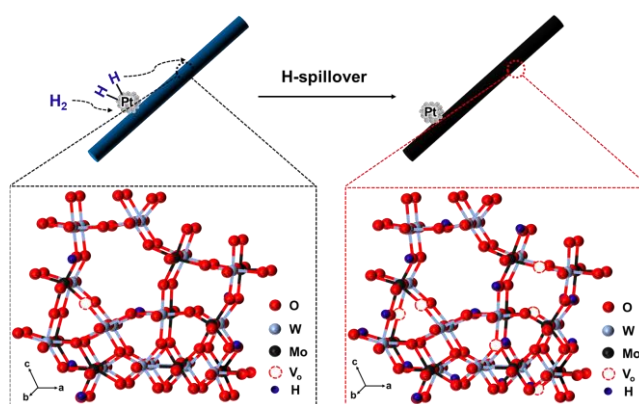
Catalytic Activity Evaluation.

The catalyst (100 mg) was placed into a stainless-steel flow reactor that was subsequently sealed with a quartz window. The catalyst was pre-reduced in a H₂ flow (20 mL min⁻¹) for 1 h at 200 °C. The temperature was then lowered to 140 °C, and a mixed gas of H₂ and CO₂ (1:1, total 20 mL min⁻¹) was introduced into the reactor to initiate the RWGS reaction. A Xe lamp (SAN-El ELECTRIC XEF-501S, $\lambda > 450 \text{ nm}$) equipped with a 450 nm cutoff filter was used to irradiate the catalyst through a quartz window from the top of the reactor during the reaction. The product gases were analyzed and quantified using online gas chromatography (Shimadzu GC-14B), equipped with a flame ionization detector, a methanizer (Shimadzu MTN-1) and an active carbon column.

Results and discussion

Structural Analysis of MoWO_y and Pt/H_xMoWO_y

In the present work, a facile solvothermal method was used to synthesize WO_y and Mo-doped WO_y nanowire. As shown in Fig. S1, the XRD peaks for the samples were all indexed to monoclinic W₁₈O₄₉ (PDF#71-2450). The Mo-doping does not alter the crystal phase of the WO_y nanowires. The pure WO_y displays a nanowire morphology with a diameter of around 5 nm (Fig. S2), which is consistent with the results of previous studies.³¹ The N₂ adsorption-desorption measurements shows that the Mo doping increases the surface area of WO_y (Fig. S3), exposing more active sites on the catalyst surface. However, the addition of an excess amount of Mo into the WO_y resulted in a decrease in the specific surface area, which is attributable to agglomeration of the nanowire (see Table S1). According to the UV-vis-NIR diffuse reflectance spectra of the samples (Fig. S4), the Mo doping led to an increase in the free carrier density and to an increase in the efficiency of polaron-to-polaron transitions in the MoWO_y(z), thereby enhancing light absorption in the Vis-NIR region.³⁰ Notably, the Pt/MoWO_y before H₂ reduction showed a noticeable photocurrent response under Vis-NIR light irradiation, whereas Pt/WO_y showed no photo response (Fig. S5). These results demonstrate that Mo doping can promote photoinduced electron production in the WO_y. As evident in the high-resolution TEM (HRTEM) images (Fig. 1b, c, d), ordered lattice fringes with an interplanar distance of 0.38 nm can be assigned to the (010) planes of WO₃, demonstrating that the Pt/H_xMoWO_y nanowire grew along the [010] direction. Fig. 1f-g reveals that the distributions of O, Mo, and W elements corresponding to the scanning transmission electron microscopy (STEM) image (Fig. 1e) of Pt/H_xMoWO_y are uniform. The weight percentages of doped Mo element and deposited Pt in WO_y were determined by inductively coupled plasma atomic emission spectroscopy (Table S2). The results show that the amount of doped Mo can be controlled during the catalyst synthesis. The Pt NPs with a diameter of around 10 nm are observed in the Pt/H_xMoWO_y (Fig. 1i). The precise size of the Pt NPs as determined by CO pulse analysis are provided in Table S3. The Pt NPs on the prepared samples exhibit similar sizes (8.9 ~ 10.7 nm), indicating that the extent of Mo-doping in WO_y has little effect on the size of the Pt NPs.



Scheme 1. Schematic of the plausible formation process of Pt/H_xMoWO_y via the H-spillover process.

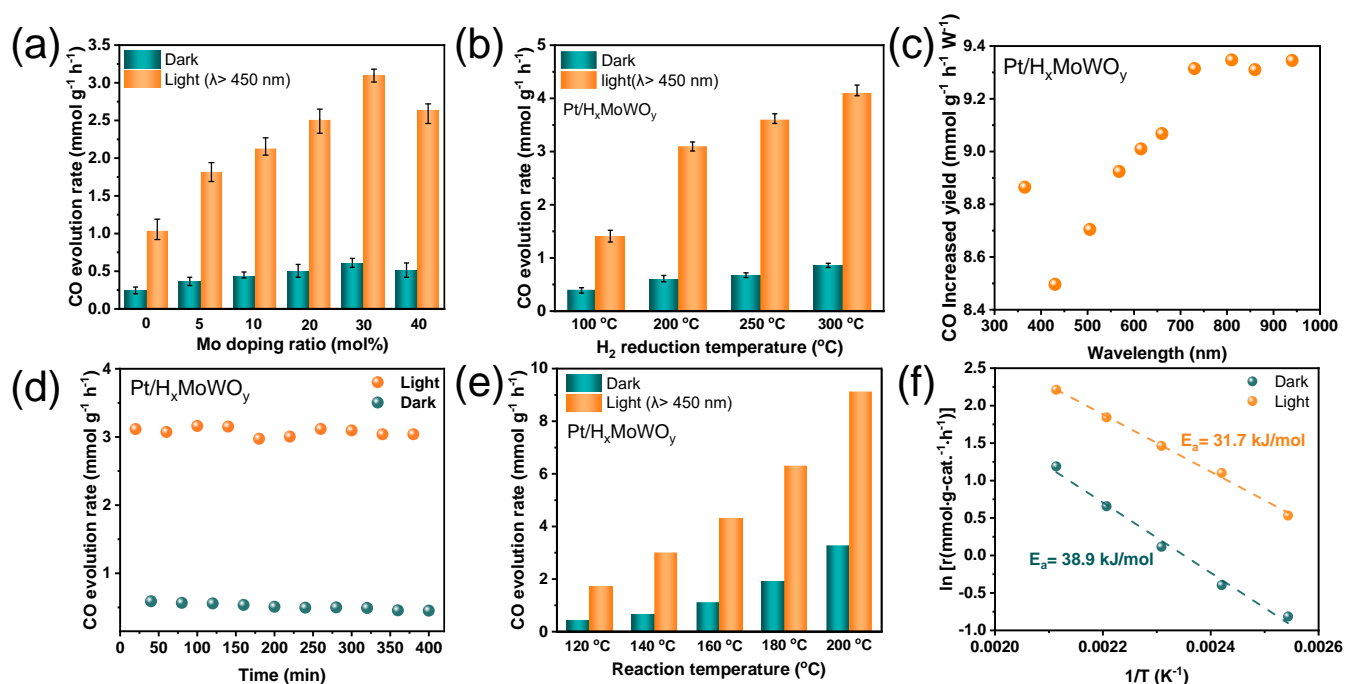


Fig. 3. Photothermal catalytic performance test in the reverse water-gas shift (RWGS) reaction under the dark condition and Vis-NIR irradiation: (a) CO production rate on Pt/H_xMoWO_y with different amount of Mo-doping, (b) H₂ reduction temperature dependence of the CO production rate on Pt/H_xMoWO_y, (c) light wavelength dependence of CO increased yield on Pt/H_xMoWO_y (LED light intensity: 155 mW cm⁻²), (d) The stability test for photothermal catalytic CO₂ reduction in a flowing system using a fixed-bed reactor system, (e) Reaction temperature dependence of the CO production rate on Pt/H_xMoWO_y, and (f) the corresponding Arrhenius plot with activation energies noted. (Reaction conditions: catalyst (0.1 g), H₂/CO₂ (1: 1, total 20 mL min⁻¹), Xe lamp (λ > 450 nm), Reaction Temp. = 140 °C, Light intensity: 0.88 W cm⁻²)

Oxygen Vacancy Formation and Reinforced Plasmonic Effect of Pt/H_xMoWO_y by H₂ Reduction.

The XRD pattern for Pt/MoWO_y (Fig. S6) shows that loading Pt onto the MoWO_y did not change the crystal phase of MoWO_y; a small peak assigned to the Pt metal is also observed. After H₂ reduction at 200 °C, the Pt/H_xMoWO_y exhibit the same crystal phase and the intensity of the Pt metal peak increased, which we attributed to reduction of the Pt NPs. The H₂-TPR profiles (Fig. S7) reveal the H-spillover process,^{41,42} where H₂ chemisorbed onto the surface of the Pt NPs generates reactive H atoms that can intercalate into the MoWO_y(z) and WO_y. The profiles for all the samples with Pt show a TPR signal at 50–350 °C, whereas the pure WO_y without Pt loading was not reduced by H₂, consistent with the results of previous works.³² H₂ consumption associated with the reduction of the WO_y support with the aid of Pt NPs was observed at 200–350 °C for the undoped Pt/WO_y, demonstrating that the process of H-intercalation into WO_y via H-spillover requires a reduction temperature higher than 200 °C. However, the Pt/MoWO_y generated a TPR signal at around 100 °C, indicating that Mo-doping facilitates H-spillover in MoWO_y at lower temperatures, thereby enabling the intercalation of H atoms and generating more defects than in pure WO_y. We investigated the surface chemical states of Pt/MoWO_y and Pt/WO_y by XPS to verify the formation of defect sites. According to XPS results of Fig. 2a and 2b, high-valence W species (W⁶⁺: 35.9 and 38.1 eV; W⁵⁺: 35.4 and 36.7 eV) were confirmed to be partially reduced to low-valence W species (W⁵⁺: 35.4 and 37.6 eV; W⁴⁺: 34.5 and 36.7

eV) upon H₂ reduction.³¹ The formation of the low-valence W⁴⁺ is assumed to be mainly due to the removal of oxygen from the lattice, leaving excess electrons in the lattice; these electrons can subsequently be captured by adjacent metal cations. The proportion of these low-valence W⁴⁺ species in Pt/H_xWO_y and Pt/H_xMoWO_y was determined to be 18% and 22%, respectively (for details, see Table S4), demonstrating that more oxygen vacancies were generated in the Pt/H_xMoWO_y than in the Pt/H_xWO_y. The Mo 3d XPS spectrum of the Pt/H_xMoWO_y shows a new peak due to low-valence Mo⁴⁺ after H₂ reduction, suggesting that oxygen vacancies were generated around the Mo species (Fig. 2c). To further confirm the changes in the local coordination structure of Pt/H_xMoWO_y catalysts, we conducted XAFS measurements. The Fourier transforms of extended XAFS (FT-EXAFS) spectra of the Mo K-edge (Fig. 2d) demonstrate that the peak associated with Mo–O bonds in the Pt/MoWO_y shifted to a higher interatomic distance (1.65 Å) after H₂ reduction. A peak associated with the Mo–(O)–Mo bonds at ~3.1 Å could not be observed because of the high dispersion of Mo in WO_y forming isolated Mo species. A similar reduction behavior for Mo species in the Pt/MoWO_y with different Mo-doping molar ratios was confirmed via the inspection of the Mo K-edge X-ray absorption near edge structure (XANES) spectra and the FT-EXAFS spectra (Fig. S8). As shown in the Pt 4f XPS spectra (Fig. S9), the Pt species in the Pt/H_xMoWO_y and Pt/H_xWO_y were found to be present as Pt⁰ NPs via H₂ reduction. Given the aforementioned information, we propose a possible formation process for H atoms insertion and oxygen vacancy generation

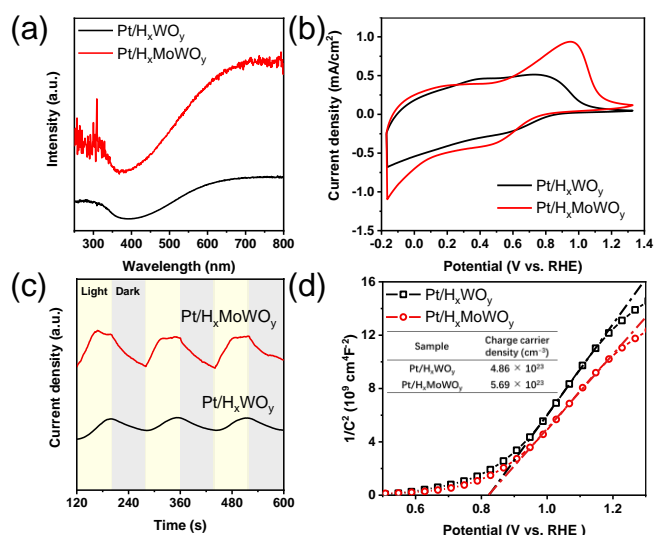


Fig. 4. (a) UV-vis-NIR diffuse reflectance spectra, (b) CV profiles, (c) photocurrent measurement and (d) Mott-Schottky plots of Pt/H_xMoWO_y and Pt/H_xWO_y (Light source: Xe lamp, Intensity = 0.88 W cm⁻², λ > 450 nm).

in the Pt/MoWO_y(z) via a H-spillover process (Scheme 1). The dopants (H⁺) and free electrons intercalate into MoWO_y during the H-spillover, which is caused by rapid dissociation of H₂ over the Pt NP surface (H₂ → 2H⁺ + 2e⁻), consequently producing large amounts of low-valence W and Mo species. As the H₂ reduction process continues, the lattice oxygen atoms around Mo are thermally expelled at around 200 °C (2H⁺ + 2e⁻ + O_{lattice} → V_O + H₂O), thereby driving the generation of a large number of oxygen vacancies. According to previous studies,^{34,38,43} the intercalation of H atoms and the introduction of oxygen vacancies into MoWO_y increase the free electron concentration, consequently causing the emergence of SPR.

Notably, the H⁺ dopants concentration and the oxygen vacancy density can be adjusted by controlling the H₂ reduction temperature. To investigate the changes in the free electron concentration and oxygen vacancy density in the Pt/MoWO_y resulting from changes in the H₂ reduction temperature, we conducted UV-vis-NIR and photoelectrochemical measurements. As shown in Fig. S10a, Pt/MoWO_y without H₂ reduction exhibited weak plasmonic absorption in the Vis-NIR region. As the temperature of H₂ reduction increased, the Pt/H_xMoWO_y after reduction at 200 °C displayed stronger plasmonic absorption, which we attributed to the increase in the concentration of free electrons in the MoWO_y. The cyclic voltammetry (CV) measurement revealed an interesting phenomenon (Fig. S10b). A strong oxidation peak was observed in Pt/H_xMoWO_y reduced at 200 °C, whereas the oxidation peak did not appear in Pt/H_xMoWO_y reduced at room temperature or in unreduced Pt/H_xMoWO_y samples, suggesting that a high H₂ reduction temperature promotes the generation of oxygen vacancies. The fact that Pt/H_xMoWO_y reduced at 200 °C exhibits the largest electrical capacity among the investigated catalysts suggests that it possesses the largest number of active sites. The cyclic voltammograms corresponding to the second CV cycle show no oxidation peak (Fig. S11) for the Pt/H_xMoWO_y-200 °C

sample, likely because of the oxidation of oxygen vacancies by the positive bias (0.6-1.1 eV) in the first CV cycle. ESR measurement was employed to detect oxygen vacancy in the prepared catalyst with different H₂ reduction temperature. As shown in Fig. S12, an obvious signal with the g values at 1.903 was observed, which was attributed to Mo⁵⁺ species.³³ The Mo⁵⁺ signal intensity increased as the H₂ reduction temperature increased, indicating that the oxygen vacancies density can be adjusted by controlling the reduction temperature. In addition, the photocurrent density of Pt/MoWO_y was enhanced as the H₂ reduction temperature was increased (Fig. S10c), indicating that the increased in the number of free electrons promotes the production of photoinduced electrons. Mott-Schottky plots (Fig. S10d) show that a higher H₂ reduction temperature caused a shift of the flat-band potential of Pt/MoWO_y in the positive potential direction, possibly because of an increase in the carrier density in the CB.³⁰ The electrochemical impedance measurement was carried out to further investigate H₂ reduction effect for the free electron concentration and oxygen vacancy density in the catalyst. As shown in Fig. S13a, Pt/H_xMoWO_y exhibited a smaller semicircle than that in Pt/MoWO_y under light irradiation. A similar phenomenon was observed in dark condition (Fig. S13b). These results indicate that Pt/H_xMoWO_y possesses a higher free electron concentration and oxygen vacancy density compared with unreduced Pt/MoWO_y, which improves the conductivity both in the bulk and semiconductor-liquid interface. On the basis of the aforementioned results, we conclude that H₂ reduction can promote defect generation (oxygen vacancies) and increase the free electrons concentration in the Pt/MoWO_y, and that these effects can easily be modulated by altering H₂ reduction temperature.

Photothermal Catalytic CO₂ Hydrogenation.

In the present work, a photothermal catalytic CO₂ hydrogenation reaction was carried out at a reaction temperature of 140 °C in a gas flow of H₂/CO₂ (10/10 mL min⁻¹) under Vis-NIR light irradiation (light source: λ > 450 nm; light intensity: 0.88 W cm⁻²). Fig. 3a shows the CO yields obtained in the RWGS reaction for a series of Pt/H_xMoWO_y(z). The catalytic activity of Pt/H_xMoWO_y(z) gradually increased with increasing amount of Mo doped into the WO_y. When Mo/W molar ratio reached 30%, the prepared catalyst displayed optimal catalytic activity with near 100% CO selectivity, and CO formation rates of 3.1 mmol h⁻¹ g⁻¹ and 0.59 mmol h⁻¹ g⁻¹ at 140 °C were obtained under Vis-NIR irradiation (λ > 450 nm) and under dark condition, respectively. The doping of excessive Mo⁵⁺ into WO_y led to nanowire agglomeration (Fig. S2), and to a decrease in the surface area (Fig. S3), which might be the main reason for the observed decrease in activity of Pt/H_xMoWO_y(40). Notably, Pt/H_xMoWO_y(30) led to a substantial CO yield enhancement by a factor of 5.1 under Vis-NIR light irradiation compared with the yield under dark conditions. This activity enhancement rate was larger than that observed for Pt/H_xWO_y (4.1fold), indicating that irradiation with Vis-NIR light greatly facilitated the RWGS reaction. The light-induced activity enhancement of other oxide-supported Pt catalysts was less substantial than that of

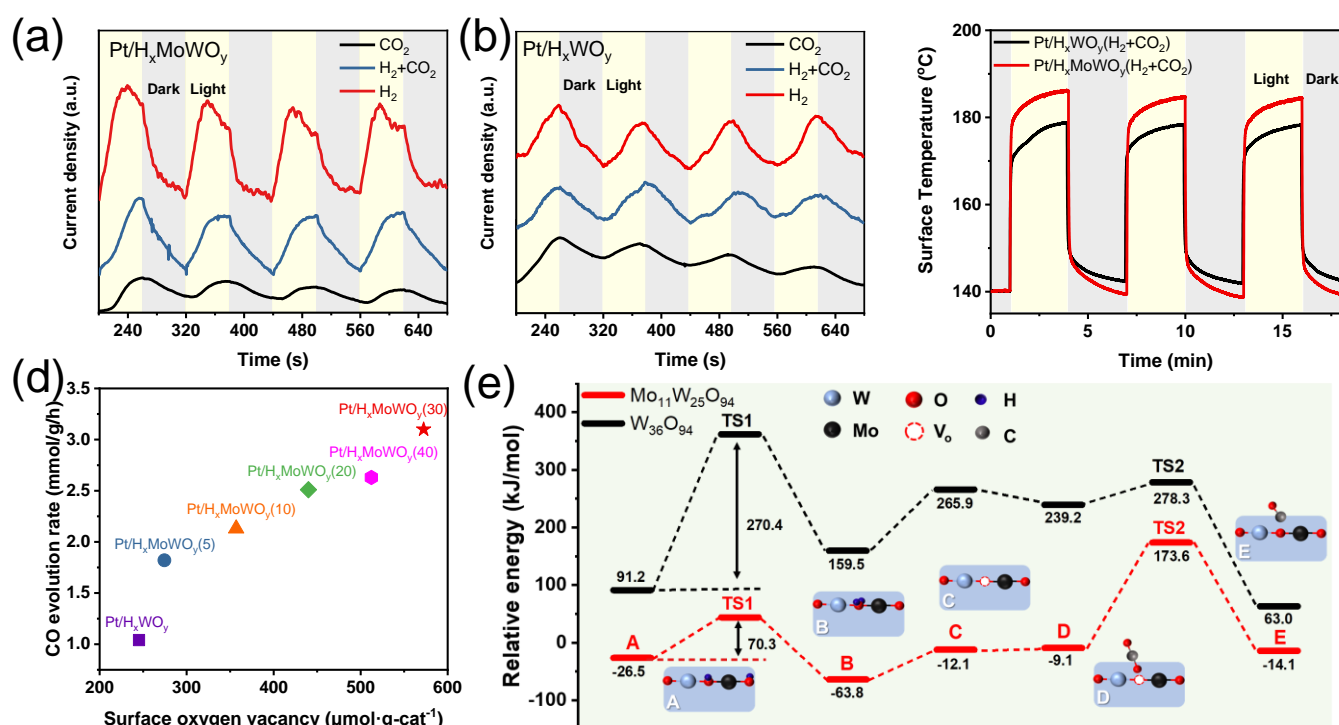


Fig. 5. Photocurrent density measurement under different atmosphere (H_2 ; H_2+CO_2 ; CO_2): (a) $\text{Pt}/\text{H}_x\text{MoWO}_y$, (b) $\text{Pt}/\text{H}_x\text{WO}_y$, (c) Surface temperature profiles of $\text{Pt}/\text{H}_x\text{MoWO}_y$ and $\text{Pt}/\text{H}_x\text{WO}_y$ in the H_2+CO_2 atmosphere under light irradiation ($\lambda > 450 \text{ nm}$). (d) The relationship between the number of surface oxygen vacancies and catalytic activity. (e) The potential energy diagram obtained by DFT calculation using models of $\text{Mo}_{11}\text{W}_{25}\text{O}_{94}$ and $\text{W}_{36}\text{O}_{94}$ and schematic illustrations of the corresponding structure models.

$\text{Pt}/\text{H}_x\text{MoWO}_y$ (Fig. S14), primarily because Pt/TiO_2 and Pt/CeO_2 catalysts do not exhibit plasmonic absorption in the Vis-NIR region. Although Pt/WO_3 (prepared using commercial WO_3) and $\text{Pt}/\text{H}_y\text{MoO}_{3-x}$ exhibit photo-enhancement under Vis-NIR light irradiation, their activities were lower than that of $\text{Pt}/\text{H}_x\text{MoWO}_y$ under Vis-NIR irradiation. The relationship between the activity and H_2 reduction temperature was also investigated. As shown in Fig. 3b, the CO yield of $\text{Pt}/\text{H}_x\text{MoWO}_y$ exhibited a substantial enhancement with increasing H_2 reduction temperature increased. Given this result and the electrochemical behaviour observed in Fig. S10, the increases in the oxygen-vacancy and free-electron concentrations in the catalyst are mainly responsible for the increased catalytic activity. The UV-vis-NIR spectra verify that the prepared catalyst exhibits strong plasmonic absorption in the NIR region ($\lambda > 700 \text{ nm}$). To explore the dependence of the CO yield on the light source, LED lamps with different emission wavelengths were used as light sources (light intensity of LED lamp: 155 mW cm^{-2}). Fig. 3c shows that the highest activity was obtained under irradiation with light with a wavelength of $730 \sim 940 \text{ nm}$, indicating that the $\text{Pt}/\text{H}_x\text{MoWO}_y$ is a suitable photothermal catalyst for NIR-light-driven CO_2 hydrogenation. The photocurrent density obtained during irradiation of $\text{Pt}/\text{H}_x\text{MoWO}_y$ with different LED lamps (940 nm, 660 nm, 505 nm) demonstrates that more photoinduced electrons were produced under 940 nm LED irradiation (Fig. S15); thus, irradiation with NIR light offers a superior photo enhancement effect. A comparison of the performance of $\text{Pt}/\text{H}_x\text{MoWO}_y$ with that of catalysts reported in previous studies

reveals that the $\text{Pt}/\text{H}_x\text{MoWO}_y$ catalyst provides an excellent CO yield relatively mild reaction condition (Table S5). This remarkable performance might be related to the plasmonic absorption, CO_2 adsorption ability, and defect (oxygen vacancy) concentration, which will be discussed later. The catalytic stability of the $\text{Pt}/\text{H}_x\text{MoWO}_y$ in a flowing system showed that the photothermal catalytic activity remained even after 7 h of reaction, indicating that the prepared catalyst exhibits good stability (Fig. 3d). To further verify the durability of the catalyst, we carried out five repeated cycling tests on the catalyst (six hours for each cycle). Fig. S16 shows that the catalyst maintains the efficient catalytic performance without any significant activity reduction. FESEM images (Fig. S17) and XRD patterns (Fig. S18) for $\text{Pt}/\text{H}_x\text{MoWO}_y$ show no differences before and after the reaction, further indicating good durability of the catalyst. In addition, $\text{Pt}/\text{H}_x\text{MoWO}_y$ exhibited an apparent decrease in activation energy from 38.9 kJ mol^{-1} in the RWGS reaction under Vis-NIR light irradiation to 31.7 kJ mol^{-1} under dark conditions (Fig. 3e, f), suggesting that light irradiation can decrease the activation energy of RWGS reactions to promote CO generation. According to the catalytic performance results, we hypothesized that Mo doping facilitates H intercalation and oxygen vacancy generation in WO_y during H_2 reduction, resulting in a catalyst that can effectively utilize Vis-NIR light energy and strongly enhances CO_2 hydrogenation to produce CO.

Role of Mo Doping in Pt/WO_y in H_2 reduction

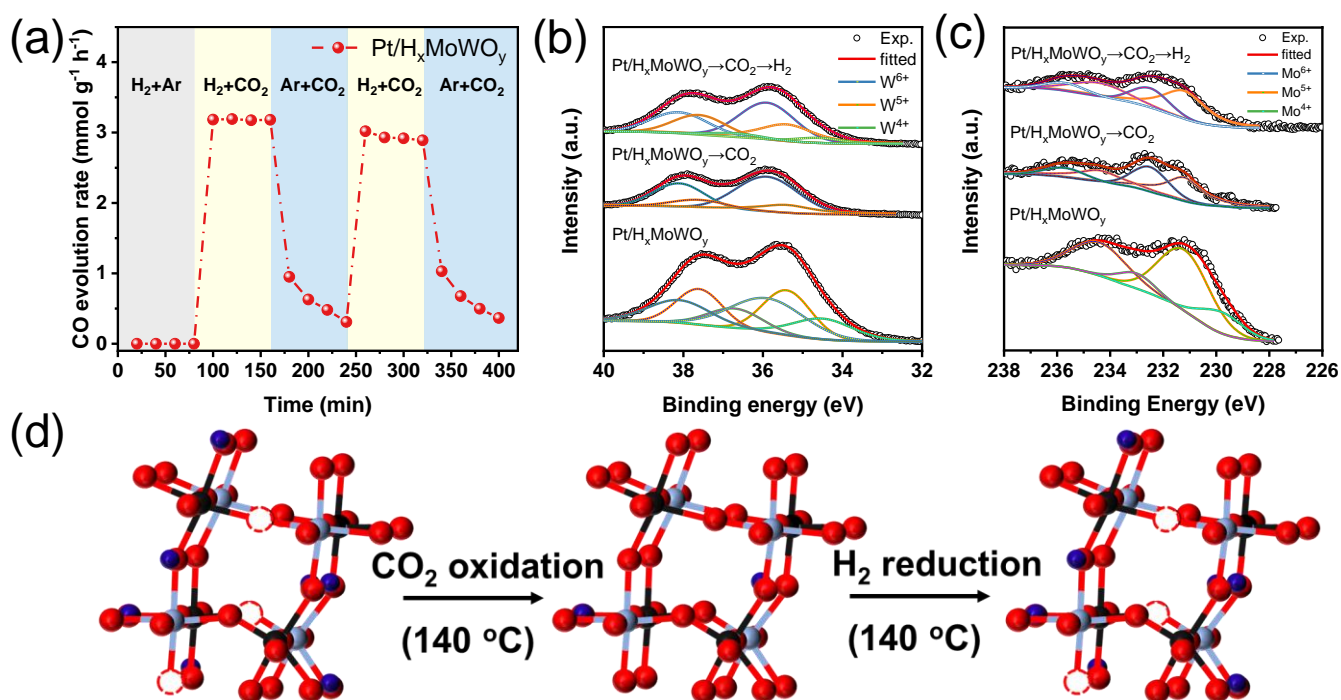


Fig. 6 (a) Gas-switching test of Pt/H_xMoWO_y for photothermal catalytic CO₂ reduction in a flowing system (Reaction conditions: catalyst (0.1 g), H₂/CO₂ (10/10 mL/min), Xe lamp ($\lambda > 450$ nm), Temp. = 140 °C, Light intensity: 0.88 W cm⁻²), XPS spectra of Pt/H_xMoWO_y, Pt/H_xMoWO_y→CO₂, Pt/H_xMoWO_y→CO₂→H₂: (b) W 4f; (c) Mo 3d. (d) Schematic illustration of the plausible process of oxygen vacancies regeneration in Pt/H_xMoWO_y.

Given the superior performance of Pt/H_xMoWO_y compared with that of other prepared catalysts, we used it as a representative sample to explore the mechanism in depth and compared it with undoped Pt/H_xWO_y. As shown in Fig. 4a, the Pt/H_xMoWO_y exhibited a stronger plasmonic absorption than the Pt/H_xWO_y, which can be ascribed to a high free electron concentration in Pt/H_xMoWO_y, indicating that Mo-doping promotes intercalation of the dopant (H⁺) into the Pt/MoWO_y during the H₂ reduction process. The CV of Pt/H_xMoWO_y shows an obvious oxidation peak compared with that of Pt/H_xWO_y (Fig. 4b), which is attributable to the generation of oxygen vacancies around the Mo atoms. In addition, the electrical capacity of Pt/H_xMoWO_y is larger than that of Pt/H_xWO_y, indicating that Mo doping introduces more defects (oxygen vacancy). These results are consistent with the XPS data analysis shown in Fig. 2a. We also characterized the photoelectrochemical properties of Pt/H_xWO_y and Pt/H_xMoWO_y by carrying out photocurrent density measurements and constructing Mott-Schottky plots to determine the charge separation efficiency and the charge carrier density. Pt/H_xMoWO_y showed a charge carrier density (5.69×10^{23} cm⁻³) greater than that for Pt/H_xWO_y (4.86×10^{23} cm⁻³) (Fig. 4d), which was associated with high free electron concentration and fast charge separation, as corroborated by photocurrent measurements (Fig. 4c). As illustrated in Fig. 5a, photocurrent tests were conducted under various gas atmospheres to investigate the efficiency of photoinduced electron transfer to the adsorbed CO₂. The photocurrent densities for Pt/H_xMoWO_y in CO₂ + H₂ and CO₂ atmospheres

were both lower than that in H₂ atmosphere; the current-density decrease rates (Eq. (3)) in flowing CO₂ + H₂ and CO₂ were 41% and 78%, respectively. The decrease in the photocurrent density was attributed to the photoinduced electrons transferring to the chemisorbed CO₂ molecules and to the consumption of oxygen vacancies. Compared with Pt/H_xMoWO_y, Pt/H_xWO_y exhibited a smaller decrease in photocurrent density in flowing CO₂ + H₂ and CO₂ (CO₂ + H₂: decrease rate of 30%, CO₂: decrease rate of 56%) (Fig. 5b), indicating that a stronger interaction between the oxygen vacancies and CO₂ molecules occurred on the surface of the Pt/H_xMoWO_y. Thus, Mo doping is assumed to favor the transfer of photoinduced electrons to the adsorbed CO₂, thereby boosting CO₂ activation and reduction. In addition to the photoinduced electrons transfer efficiency and intrinsic CO₂ activation ability, the photothermal conversion efficiency of catalysts under light irradiation strongly influences the catalytic performance. A radiation thermometer was used to measure the surface temperature of the catalysts during the reaction. As shown in Fig. 5c, the surface temperature of Pt/H_xMoWO_y rose from 140 °C to 186 °C after 3 mins of light irradiation (Intensity = 0.88 W cm⁻², $\lambda > 450$ nm), which was 9 °C higher than that for Pt/H_xWO_y (from 140 °C to 177 °C). The high concentration free electrons can lead to a high probability of photogenerated carrier recombination, which enhances the photothermal conversion efficiency.⁴⁴ The RWGS reaction was examined under dark conditions at a reaction temperature of 186 °C (Fig. S19). The increase in activity caused by increasing the reaction temperature to 186 °C accounted for

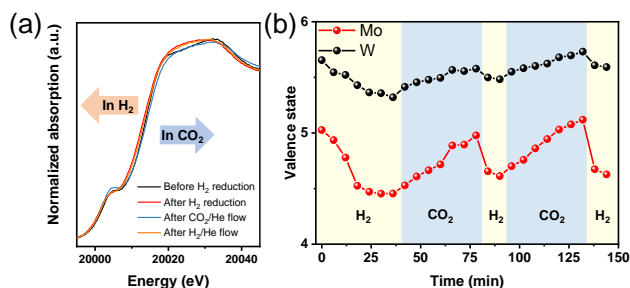


Figure 7. (a) *In situ* Mo K-edge XANES spectra of Pt/MoWO_y; before H₂ reduction, after H₂ reduction under a flow of 20% H₂/He (reduction temp.: 200 °C), after a subsequent flow of 20% CO₂/He and subsequent flow of 20% H₂/He (measured at 140 °C). (b) Change of valence state of the Mo and W species during the *in situ* XAFS measurement. The valence state was determined by a linear interpolation method.

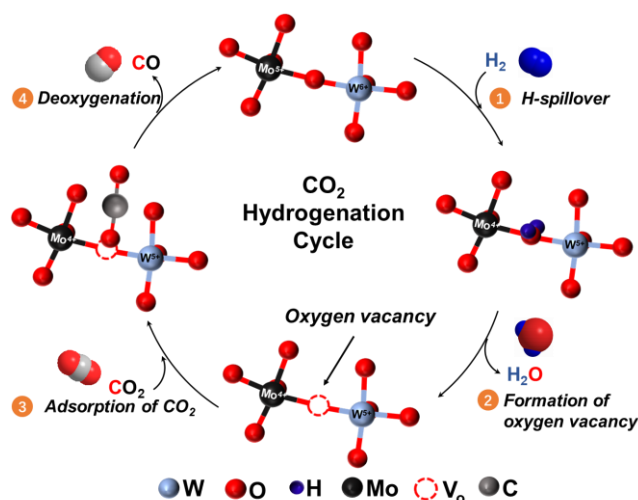
90% of the light-driven activity enhancement observed at 140 °C, indicating that the thermal effect of light irradiation was the main factor in increasing activity, rather than the direct reduction of CO₂ molecules by hot electrons.

To further clarify the relationship between the number of oxygen vacancies and the Mo-doping amount in the Pt/H_xMoWO_y(z), we employed a model reaction to determine the number of surface oxygen vacancies in the prepared catalysts.³⁷ As shown in Fig. 5d, Pt/H_xMoWO_y generated the largest amount of diphenyl sulfide (572 μmol g⁻¹-cat, for details, see Table S6), indicating that Pt/H_xMoWO_y has the largest number of surface oxygen vacancies among all the samples, and that the amount of oxygen vacancies are related to the catalytic performance. The CO₂ adsorption isotherms also indicated that Pt/H_xMoWO_y could adsorb more CO₂ molecules than Pt/H_xWO_y because of its greater number of generated surface oxygen vacancies (Fig. S20). Based on the structural information obtained in the previously described experiments, we carried out DFT calculations using models of Mo₁₁W₂₅O₉₄ and W₃₆O₉₄ to simulate a possible reaction pathway for CO generation. Fig. 5e shows the calculated stepwise energy diagrams for CO generation on Mo₁₁W₂₅O₉₄ and W₃₆O₉₄ (the detailed structure models for each step are shown in Fig. S21 and S22). For the pristine W₃₆O₉₄ model, the oxygen vacancy formation process needs to overcome a high energy barrier of 270.4 kJ mol⁻¹ (TS1), and the energy level substantially increases after an oxygen vacancy is formed, indicating that the oxygen vacancy formation process in pure WO_y is difficult and unstable. When Mo is doped into the WO_y, the energy barrier for oxygen vacancy formation decreases dramatically (TS1, 70.3 kJ mol⁻¹), the Mo₁₁W₂₅O₉₃ containing an oxygen vacancy in a unit cell maintains a lower relative energy for each step compared with those calculated for W₃₆O₉₄. This result illustrates that the doping Mo into WO_y boosts oxygen vacancy formation and stability during H₂ reduction, thereby facilitating the CO generation in the subsequent reaction step. The aforementioned results demonstrate that the Mo dopant in WO_y performs two roles: (1) promoting the formation of oxygen vacancies and the intercalation of H atoms in Pt/MoWO_y during the H₂ reduction, which enhance the plasmonic absorption and photothermal conversion efficiency under Vis-NIR irradiation, and (2) promoting the formation of oxygen vacancies in Mo-O-

W bond which improves the catalyst's ability to activate reduce CO₂, where photoinduced electrons are transferred from the undercoordinated Mo(W) sites to chemisorbed CO₂.

Reaction mechanism

A gas-switching study in photothermal catalytic CO₂ reduction was performed. As shown in Fig. 6a, the catalytic performance exhibited a progressive decrease in the absence of H₂. By contrast, the catalyst showed a constant CO evolution rate when H₂ was present, likely because of the continuous regeneration of oxygen vacancies under the H₂ atmosphere. In addition, the CO was not produced in a flow of Ar + H₂ and CO generation could be detected after the gas was switched from Ar + H₂ to CO₂ + H₂, demonstrating that the generated CO was solely derived from CO₂. The XPS measurement were employed to monitor changes in the surface oxidation states of Pt/H_xMoWO_y during the reaction. As shown in Fig. 6b, after the Pt/H_xMoWO_y was reacted with CO₂ at 140 °C for 2 h under the dark conditions, the W 4f XPS spectra showed a decrease in the proportion of the (W⁴⁺+W⁵⁺)/W_{total} and the Mo⁴⁺ peak disappeared from the Mo 3d spectra (Fig. 6c). These results illustrate that the oxygen vacancies in the Pt/H_xMoWO_y were occupied by CO₂ during the reaction. In a subsequent experiment, the Pt/H_xMoWO_y that reacted with CO₂ was reduced by H₂ at 140 °C for 1 h again. The XPS spectra show that the peak intensity of W⁵⁺ and W⁴⁺ increased, and the proportion of Mo⁵⁺ increased, indicating that H₂ reduction can regenerate the oxygen vacancies (for details, see Table S7 and S8). A plausible process for oxygen vacancy regeneration was illustrated in Fig. 6d. To further understand the reaction mechanism and role of Mo-doping during photothermal catalytic CO₂ hydrogenation, *in situ* XAFS measurement were carried out. Fig. 7a shows XANES spectra in the Mo K-edge region for the sample of Pt/MoWO_y before and after H₂ reduction at 200 °C, along with other spectra acquired after the sample was exposed to H₂ and CO₂ at 140 °C. The pre-edge absorption position of Pt/MoWO_y after H₂ reduction strongly shifted toward the lower energy region compared with that before H₂ reduction, which was approximately the same as the pre-edge absorption position of monoclinic MoO₂. After the introduction of CO₂/He gas flow at 140 °C, the pre-edge absorption shifted to higher energy, indicating that Mo species in the samples were oxidized by CO₂. When the gas flow was switched to H₂/He, the absorption edge shifted back to the lower energy region, indicating the re-reduction of the Mo species. By contrast, this phenomenon was hardly observed in the W L3-edge region (Fig. S23). The linear interpolation method was used to trace the change in the average valence state for Mo and W in Pt/H_xMoWO_y, during the *in situ* XAFS measurement and the results were plotted as a function of time. As shown in Fig. 7b, the valence state of Mo species exhibited a reversible change under the H₂/CO₂ gas flow, demonstrating that a redox event occurred on the Mo species during the CO₂ reduction. The Mo species are initially reduced by H₂ to generate oxygen vacancy. A CO₂ molecule is subsequently adsorbed at an oxygen vacancy around the under-coordinated Mo⁴⁺ sites to produce CO, which is accompanied by oxidation of



Scheme 2. Proposed reaction mechanism of CO₂ hydrogenation to produce CO over Pt/H_xMoWO_y catalyst.

the Mo species and consumption of an oxygen vacancy. Finally, H₂ re-reduces the Mo species to regenerate the oxygen vacancy. Notably, the valence state of W species changed slightly during the measurement, likely because the oxygen vacancies were mainly generated around the Mo species. On the basis of our comprehensive analysis of the experimental results, we propose a potential reaction pathway via the oxygen vacancy-mediated “reverse Mars–van Kreveren” mechanism.^{45,46} As shown in Scheme 2, H₂ dissociation first occurs on the surface of the Pt NPs, driving the intercalation of H atoms and the generation of oxygen vacancies in the Pt/MoWO_y via H-spillover (steps 1 and 2). The oxygen vacancies effectively adsorb CO₂ molecules, and the adjacent undercoordinated low-valence Mo and W centers (Mo⁴⁺/Mo⁵⁺; W⁴⁺/W⁵⁺) can activate the adsorbed CO₂ via electrons transfer, inducing polarization of the CO₂, which leads to weakening and dissociation of the C=O bond in CO₂. The CO is formed in conjunction with the consumption of oxygen vacancies (step 3). The H atoms then intercalate into the Pt/H_xMoWO_y, again to regenerate the oxygen vacancies (step 4). The whole reaction process displays a reversible redox property on Pt/H_xMoWO_y, realizing a photothermal catalytic cycle.

Conclusion

In conclusion, a Pt/H_xMoWO_y catalyst with intense plasmonic absorption in the Vis–NIR region displayed an excellent photothermal catalytic performance in the RWGS reaction (3.1 mmol h⁻¹ g⁻¹) under relatively mild reaction conditions. This catalytic activity was much higher than that of the un-doped Pt/H_xWO_y catalyst (1.04 mmol h⁻¹ g⁻¹). The Pt/H_xMoWO_y catalyst developed via H₂ reduction process offers a significant activity enhancement in the RWGS reaction for the following reasons: (i) Mo doping improves the concentration of dopants (H⁺) and oxygen vacancies in Pt/MoWO_y via H-spillover process, thereby improving the plasmonic absorption properties and the CO₂ adsorption capability; (ii) the existence of Mo–O–W bonds increases the efficiency of photoinduced electron transfer from undercoordinated Mo(W) sites to chemisorbed CO₂; and (iii) an increased probability of nonradiative recombination of SPR-induced

excited electrons promotes the photothermal conversion, thereby facilitating activation of the adsorbed CO₂. In addition, a “reverse Mars–van Kreveren” mechanism based on oxygen vacancy regeneration was proposed. This mechanism is achieved by the synergistic interaction between reducible Mo–O–W species as a CO₂ activation centre and a Pt NP as a H₂ activation centre. We anticipate that our work will provide a promising technique for tuning the physicochemical properties of catalysts to improve the efficiency of CO₂ reduction, and assists in the inherent understanding of oxygen vacancy-mediated catalytic CO₂ conversion, and photothermal CO₂ conversion.

Conflicts of interest

There are no conflicts to declare

Acknowledgements

The present work was supported by JST, PRESTO (Grant no. JPMJPR19T3), Japan. A part of this work was supported by Kawasaki Heavy Industries, Ltd. and the Element Strategy Initiative of MEXT, Japan (No. JPMXP0112101003). The synchrotron radiation experiments for XAFS measurements were performed at the BL01B1 beamline in SPring-8 with approval from JASRI (Nos. 2020A1064, 2021B1090).

Notes and references

- J. R. Ran, M. Jaroniec, S. Z. Qiao, *Adv. Mater.* 2018, **30** (7), 1704649 (31 pages).
- J. Albero, Y. Peng, H. García, Photocatalytic CO₂ Reduction to C²⁺ Products. *ACS Catal.* 2020, **10** (10), 5734–5749.
- Y. Dong, P. Duchesne, A. Mohan, K. K. Ghuman, P. Kant, L. Hurtado, U. Ulmer, J. Y. Y. Loh, A. A. Tountas, L. Wang, A. Jelle, M. Xia, R. Dittmeyer, G. A. Ozin, *Chem. Soc. Rev.* 2020, **49** (16), 5648–5663.
- J. Wang, T. Heil, B. Zhu, C. W. Tung, J. Yu, H. M. Chen, M. Antonietti, S. Cao, *ACS Nano* 2020, **14** (7), 8584–8593.
- L. Han, S. Song, M. Liu, S. Yao, Z. Liang, H. Cheng, Z. Ren, W. Liu, R. Lin, G. Qi, X. Liu, Q. Wu, J. Luo, H. L. Xin, *J. Am. Chem. Soc.* 2020, **142** (29), 12563–12567.
- T. N. Nguyen, M. Salehi, Q. V. Le, A. Seifitokaldani, C. T. Dinh, *ACS Catal.* 2020, **10** (17), 10068–10095.
- P. Boldrin, J. R. Gallagher, G. B. Combes, D. I. Enache, D. James, P. R. Ellis, G. Kelly, J. B. Claridge, M. J. Rosseinsky, *Chem. Sci.* 2015, **6** (2), 935–944.
- M. D. Porosoff, B. Yan, J. G. Chen, *Energy Environ. Sci.* 2016, **9** (1), 62–73.
- D. J. Pettigrew, D. L. Trimm, N. W. Cant, *Catal. Lett.* 1994, **28** (2), 313–319.
- M. Saito, J. Wu, K. Tomoda, I. Takahara, K. Murata, *Catal. Lett.* 2002, **83** (1), 1–4.
- J. A. Loiland, M. J. Wulfers, N. S. Marinkovic, R. F. Lobo, *Catal. Sci. Technol.* 2016, **6** (14), 5267–5279.
- M. S. Frei, C. Mondelli, R. García-Muelas, K. S. Kley, B. Puértolas, N. López, O. V. Safonova, J. A. Stewart, D. C. Ferré, D.; J. Pérez-Ramírez, *Nat. Commun.* 2019, **10** (1), 3377.
- T. Riedel, G. Schaub, K. W. Jun, K. W. Lee, *Ind. Eng. Chem. Res.* 2001, **40** (5), 1355–1363.
- A. Aitbekova, L. Wu, C. J. Wrasman, A. Boubnov, A. S. Hoffman, E. D. Goodman, S. R. Bare, M. Cargnello, *J. Am. Chem. Soc.* 2018, **140** (42), 13736–13745.

- 15 M. Ghossoub, M. Xia, P. N. Duchesne, D. Segal, G. A. Ozin, *Energy & Environmental Science* 2019, **12** (4), 1122-1142.
- 16 Y. Qi, J. Jiang, X. Liang, S. Ouyang, W. Mi, S. Ning, L. Zhao, J. H. Ye, *Adv. Funct. Mater.* 2021, **31** (22), 2100908. (8 pages)
- 17 Z. Wu, C. Li, Z. Li, K. Feng, M. Cai, D. Zhang, S. Wang, M. Chu, C. Zhang, J. Shen, Z. Huang, Y. Xiao, G. A. Ozin, X. Zhang, L. He, *ACS Nano* 2021, **15** (3), 5696-5705.
- 18 T. Li, L. Tan, Y. Zhao and Y.-F. Song, *Chemical Engineering Science*, 2021, **245**, 116839 (8 pages).
- 19 Y. Zhao, W. Gao, S. Li, G. R. Williams, A. H. Mahadi and D. Ma, *Joule*, 2019, **3**, 920-937.
- 20 J. Song, Z. F. Huang, L. Pan, J. J. Zou, X. Zhang, L. Wang, *ACS Catal.* 2015, **5** (11), 6594-6599.
- 21 C. Hoang-Van, O. Zegaoui, *Applied Catalysis A: General* 1997, **164** (1-2), 91-103.
- 22 T. J. Thibodeau, A. S. Canney, W. J. DeSisto, M. C. Wheeler, F. G. Amar, B. G. Frederick, *Applied Catalysis A: General* 2010, **388** (1-2), 86-95.
- 23 G. Prusty, J. T. Lee, S. Seifert, B. B. Muhoberac, R. Sardar, *J. Am. Chem. Soc.* 2020, **142** (13), 5938-5942.
- 24 S. Sun, M. Watanabe, J. Wu, Q. An, T. Ishihara, *J. Am. Chem. Soc.* 2018, **140** (20), 6474-6482.
- 25 Y. F. Li, N. Soheilnia, M. Greiner, U. Ulmer, T. Wood, A. A. Jelle, Y. C. Dong, A. P. Y. W. Wong, A. J. Jia, G. A. Ozin, *ACS Appl. Mater. Interfaces* 2019, **11** (6), 5610-5615.
- 26 A. M. Schimpf, S. T. Ochsenein, R. Buonsanti, D. J. Milliron, D. R. Gamelin, *Chem. Commun.* 2012, **48** (75), 9352-9354.
- 27 A. Šutka, M. Timusk, N. Döbelin, R. Pärna, M. Visnapuu, U. Joost, T. Käämbre, V. Kisand, K. Saal, M. A. Knite, *RSC Adv.* 2015, **5** (78), 63846-63852.
- 28 T. Wang, P. V. Radovanovic, *J. Phys. Chem. C* 2011, **115** (2), 406-413.
- 29 A. M. Schimpf, S. D. Lounis, E. L. Runnerstrom, D. J. Milliron, D. R. Gamelin, *J. Am. Chem. Soc.* 2015, **137** (1), 518-524.
- 30 M. Shi, X. Tong, W. Li, J. Fang, L. Chen, C. Ma, *ACS Appl. Mater. Interfaces* 2017, **9** (40), 34990-35000.
- 31 Z. Xiong, Z. Lei, S. Ma, X. Chen, B. Gong, Y. Zhao, J. Zhang, C. Zheng, J. C. S. Wu, *Appl. Catal. B-Environ.* 2017, **219**, 412-424.
- 32 H. Wang, L. Zhang, K. Wang, X. Sun, W. Wang, *Appl. Catal. B-Environ.* 2019, **243**, 771-779.
- 33 N. Zhang, A. Jalil, D. Wu, S. Chen, Y. Liu, C. Gao, W. Ye, Z. Qi, H. Ju, C. Wang, X. Wu, L. Song, J. Zhu, Y. Xiong, *J. Am. Chem. Soc.* 2018, **140** (30), 9434-9443.
- 34 H. F. Cheng, M. Wen, X. Ma, Y. Kuwahara, K. Mori, Y. Dai, B. B. Huang, H. Yamashita, *J. Am. Chem. Soc.* 2016, **138** (29), 9316-9324.
- 35 H. F. Cheng, T. Kamegawa, K. Mori, H. Yamashita, *Angew. Chem. Int. Edit.* 2014, **53** (11), 2910-2914.
- 36 H. F. Cheng, X. Qian, Y. Kuwahara, K. Mori, H. Yamashita, *Adv. Mater.* 2015, **27** (31), 4616-4621.
- 37 Y. Kuwahara, Y. Yoshimura, K. Haematsu, H. Yamashita, *J. Am. Chem. Soc.* 2018, **140** (29), 9203-9210.
- 38 Y. Kuwahara, T. Mihogi, K. Hamahara, K. Kusu, H. Kobayashi, H. Yamashita, *Chem. Sci.* 2021, **12** (29), 9902-9915.
- 39 H. Ge, Y. Kuwahara, K. Kusu, H. Yamashita, *J. Mater. Chem. A* 2021, **9** (24), 13898-13907.
- 40 Y. Liu, X. Dong, Q. Yuan, J. Liang, Y. Zhou, X. Qu, B. Dong, *Colloid Surface A* 2021, **621**, 126582 (8 pages).
- 41 R. Prins, *Chem. Rev.* 2012, **112** (5), 2714-2738.
- 42 S. Ladas, *J. Catal.* 1978, **53** (3), 356-365.
- 43 M. Vasilopoulou, A. M. Douvas, D. G. Georgiadou, L. C. Palilis, S. Kennou, L. Sygellou, A. Soutlati, I. Kostis, G. Papadimitropoulos, D. Davazoglou, P. Argitis, *J. Am. Chem. Soc.* 2012, **134** (39), 16178-16187.
- 44 R. Long, Y. Li, L. Song, Y. Xiong, *Small* 2015, **11** (32), 3873-3889.
- 45 A. V. Mironenko, D. G. Vlachos, *J. Am. Chem. Soc.* 2016, **138** (26), 8104-8113.
- 46 L. F. Bobadilla, J. L. Santos, S. Ivanova, J. A. Odriozola, A. Urakawa, *ACS Catal.* 2018, **8** (8), 7455-7467.